Soft Matter

ROYAL SOCIETY OF CHEMISTRY

PAPER

View Article Online
View Journal | View Issue

Check for updates

Cite this: *Soft Matter*, 2023, **19**, 776

Received 30th September 2022,
Accepted 22nd December 2022

DOI: 10.1039/d2sm01307j

rsc.li/soft-matter-journal

Influence of surface viscosities on the electrodeformation of a prolate viscous drop

H. Nganguia,[a] D. Das,[b] O. S. Pak[c] and Y.-N. Young*[d]

Contaminants and other agents are often present at the interface between two fluids, giving rise to rheological properties such as surface shear and dilatational viscosities. The dynamics of viscous drops with interfacial viscosities has attracted greater interest in recent years, due to the influence of surface rheology on deformation and the surrounding flows. We investigate the effects of shear and dilatational viscosities on the electro-deformation of a viscous drop using the Taylor–Melcher leaky dielectric model. We use a large deformation analysis to derive an ordinary differential equation for the drop shape. Our model elucidates the contributions of each force to the overall deformation of the drop and reveals a rich range of dynamic behaviors that show the effects of surface viscosities and their dependence on rheological and electrical properties of the system. We also examine the physical mechanisms underlying the observed behaviors by analyzing the surface dilatation and surface deformation.

1 Introduction

Electric fields are increasingly being employed to manipulate suspensions of deformable particles in biomedical applications (separation and detection of infected blood cells, DNA and protein molecules), drug delivery (electroporation based therapies), and many other biologically related applications. In petroleum engineering, electric fields are used to separate mixed emulsions. In these settings, naturally occurring or added surfactants often act as demulsifiers and stabilizing agents for the emulsion.

The effect of electric fields on a clean viscous drop is now relatively well understood.[1] For a leaky dielectric drop freely suspended in another leaky dielectric fluid, the bulk charge neutralizes on a fast timescale while "free" charges accumulate on (and move along) the drop surface. In this physical regime, the full electrokinetic transport model in a viscous solvent can be described by a charge-diffusion model that can be further reduced to the Taylor–Melcher leaky dielectric model.[2] In many physics and engineering applications with moderately dissolvable electrolytes, the Taylor–Melcher leaky dielectric model can capture the deformation of a viscous drop in both dielectric[3,4] and conducting media.[5,6] In the Taylor–Melcher model, the balance between the electric stress and the hydrodynamic stress on the drop surface gives rise to a drop shape and a flow field that can be parametrized by the conductivity ratio and the permittivity ratio.[7] Under a small electric field, a steady equilibrium drop shape exists due to the balance between the electric and hydrodynamic stresses.[8–10] For a sufficiently large electric field, instabilities arise and the drop keeps deforming until it eventually breaks up into smaller drops.[11,12] The Taylor–Melcher model has been extended in recent years to include the effects of charge relaxation,[13] charge convection,[14–17] drop shapes,[18–21] drop instabilities,[10,22–27] and Marangoni stresses.[28–31]

Interfacial rheology is characterized by a shear viscosity and a dilatational viscosity on the drop interface, and may arise for drops covered with colloidal particles and proteins,[32,33] surfactants,[34] and as a property of vesicles' membrane viscosity.[33,35] Studies show a rich range of dynamics over various physical settings as a result of interfacial rheology. Its influence on deformation has been investigated for drops in a linear flow and shown to affect the critical capillary number for drop breakup.[36–38] Numerical simulations have also been conducted to determine the influence of interfacial rheology in shear[39,40] and extensional flows. For the extensional flow, Herrada *et al.*[34] found that although surface velocity is reduced, the surface viscosities have greater effect on drop breakup, and only minimal effect on the equilibrium deformation. Under the same flow, Singh and Narsimhan[41,42] showed that the dilatational viscosity led to instability, and the shear viscosity acted to stabilize the drop. Surface viscosities have also been found to alter the stability of viscous fingering[43] as well as play a role in pinch-off dynamics.[44–46]

---

[a] *Department of Mathematics, Towson University, Towson, MD 21252, USA. E-mail: hnganguia@towson.edu*
[b] *Department of Mathematics and Statistics, University of Strathclyde, Glasgow, UK. E-mail: debasish.das@strath.ac.uk*
[c] *Department of Mechanical Engineering, Santa Clara University, Santa Clara, CA 95053, USA. E-mail: opak@scu.edu*
[d] *Department of Mathematical Sciences, New Jersey Institute of Technology, Newark, NJ 07102, USA. E-mail: yyoung@njit.edu*

Recent studies have also begun to investigate the effects of interfacial rheology on the dynamics of a viscous drop in an electric field. Mandal *et al.*[47] considered a leaky dielectric drop and obtained analytical solutions using the small deformation analysis. In comparison to the clean drop case, they showed that dilatational viscosity yields larger deformation, while shear viscosity yields smaller deformation. Han *et al.*[48] instead considered the case of a conducting drop and concluded that dilatational viscosity only changes the transient dynamic of the drop, leaving the steady state deformation unchanged as the dilatational viscosity increases. While these recent findings have revealed how interfacial viscosities can alter electro-deformation of drops in different manners, the results are limited to the small deformation analysis of a leaky dielectric drop or numerical simulations of a conducting drop with only surface dilatational viscosity.

For fluid flow driven by an electric field, charges accumulate at the drop surface that separates media with different electric properties. Because of the conductivity and permittivity mismatch between the interior and exterior fluids, the electric field acting on the surface charges generate a Maxwell stress that induces fluid flow. By tuning the electric properties, one can control the circulation in and around the drop: when the interior fluid is less conducting than the exterior one, the fluid flow is pole-to-equator. Likewise, one obtains an equator-to-pole flow when the interior fluid is more conducting than the exterior one.[28,49,50] To examine the influence of these flow variations and to present a more comprehensive analysis, in this work we go beyond the small deformation regime and examine the effect of interfacial viscosities on large electro-deformations of both leaky dielectric and conducting drops *via* a spheroidal model.[18,19] Our results provide predictions in the practically significant regime of large drop deformations and shed light on the physical mechanisms underlying the observed electrohydrodynamic behaviors.

This paper is organized as follows. In Section 2, we present the physical problem, governing equations, and derive the model for drop deformation. We discuss the main findings in Section 3, where we first report various effects of surface rheology on deformation (Section 3.2); we then propose physical mechanisms behind the observations (Section 3.3). Finally, we summarize our results and outlook in Section 4.

2 Mathematical formulation

We consider a viscous drop with interfacial viscosities immersed in a leaky dielectric fluid as shown in Fig. 1(a). Each fluid is characterized by the fluid viscosity μ, dielectric permittivity ε, and conductivity σ with the subscript denoting interior (1) or exterior (2) fluid. In this work the subscript "r" denotes the ratio between exterior and interior quantities: $\mu_r = \mu_2/\mu_1$, $\varepsilon_r = \varepsilon_2/\varepsilon_1$, and $\sigma_r = \sigma_2/\sigma_1$. Typical applications of leaky dielectric fluids involve drops of mm size under an electric field strength of kV cm^{-1}.[4,8,18,50–53] Hence we assume that the fluid flow in this system is in the creeping flow regime with negligible inertia. Moreover, the flow around drops in electric field depend on the electric ratios σ_r and ε_r.[12,54] Drops are categorized as prolate 'A' or prolate 'B'. As illustrated in Fig. 1(b), they differ by the circulation inside the drops: counterclockwise in the first quadrant (equator-to-pole) for prolate 'A' ($\sigma_r/\varepsilon_r < 1$), and clockwise (pole-to-equator) for prolate 'B' ($\sigma_r/\varepsilon_r > 1$). The electric tangential stress vanishes for $\sigma_r/\varepsilon_r = 1$, and the drop remains spherical.

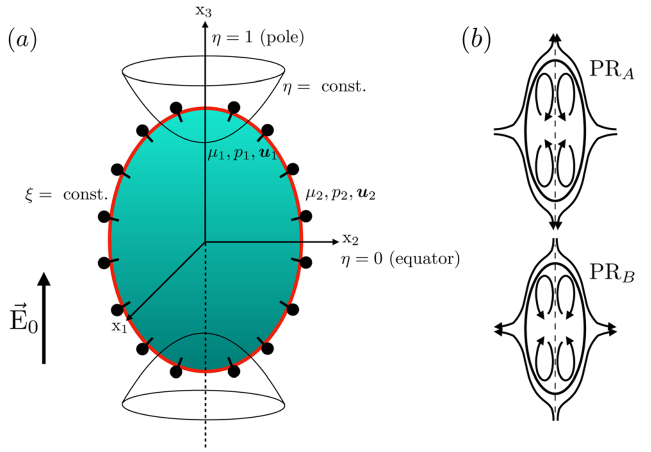

Fig. 1 (a) Sketch of the problem: an axisymmetric leaky dielectric viscous drop immersed in another dielectric fluid, with an external electric field E_0 in the z direction. The bead-rod particles represent the rheological properties of the interface (shear and dilatation). (b) Two modes of prolate shape exist: prolate 'A' (PR$_A$) with a counterclockwise circulation in the first quadrant, and prolate 'B' (PR$_B$) with a clockwise circulation in the first quadrant.

2.1 Governing equations

The fluids are governed by the incompressible Stokes equation,

$$-\nabla p_j + \mu_j \nabla^2 u_j = 0, \quad \nabla \cdot u_j = 0 \tag{1}$$

where $j = 1$ or $j = 2$ denote the drop and continuous phases, respectively, p is the pressure, and $\boldsymbol{u}$ is the velocity field. In the far-field the flow is quiescent,

$$\boldsymbol{u}_2(\boldsymbol{x} \to \infty) = 0. \tag{2}$$

The electric field $\mathbf{E}_j = -\nabla\phi_j$, where ϕ_j is the electric potential that satisfies the Laplace equation,

$$\nabla^2\phi_j = 0. \tag{3}$$

Far away from the drop surface the electric field is the imposed electric field.

$$-\nabla\phi_2 = E_0\boldsymbol{z}. \tag{4}$$

At the drop interface, boundary conditions are imposed for the electric potential ϕ, and the flow field $\boldsymbol{u}$. The electric potential is continuous and the total current is conserved,

$$[\![\phi]\!] = 0, \quad [\![\sigma\nabla\phi\cdot\boldsymbol{n}]\!] = 0, \tag{5}$$

where $[\![\cdot]\!]$ denotes the jump between outside and inside quantities. Generally, the jump in the Ohmic current, $[\![\sigma\nabla\phi\cdot\boldsymbol{n}]\!]$ is balanced by charge relaxation and charge convection.[7] The effects of these dynamics on the transient behavior of drops,[13] and on equilibrium deformation,[14,17,55] have been investigated analytically and numerically in the context of drops electrohydrodynamics. For a clean drop, both charge relaxation and convection can yield transient shape transitions and/or overshoot. However, charge relaxation does not affect the equilibrium deformation,[13] while charge convection effects depend on the electric Reynolds number.[17,56] In regard to our study, any effects of charge relaxation and convection will be transitory (affecting Fig. 5–8 in Section 3). Moreover, we anticipate a small quantitative change in the equilibrium deformations (due to charge convection). To further justify the omission of charge relaxation and convection, we note that these effects are driven by the Saville ($\mathrm{Sa} = \tau_c/\tau_p$)[7,14] and electric Reynold ($\mathrm{Re_E} = \tau_c/\tau_F$)[7,17,56] numbers, respectively, where $\tau_{c,j} = \varepsilon_j/\sigma_j$ is the charging time scale, $\tau_{p,j} = \mu_j r_0/\gamma$ is a characteristic hydrodynamic time scale, and $\tau_F = \mu_1/\varepsilon_2 E_0{}^2$ is a convective flow time. Using the experimental data[18] for an aqueous KCl drop ($\sigma_1 = 8 \times 10^{12}$ pS m^{-1}, $\varepsilon_1 = 68.9 \times 8.85$ pF m^{-1}, $\mu_1 = 0.81 \times 10^{-3}$ Pa s^{-1}) in epoxidized linseed oil ($\sigma_2 = 1.46 \times 10^3$ pS m^{-1}, $\varepsilon_2 = 6.18 \times 8.85$ pF m^{-1}, $\mu_2 = 339 \times 10^{-3}$ Pa s^{-1}); we estimate $\tau_c \approx 7.6 \times 10^{-11}$ s, $\tau_p \approx 2.9 \times 10^{-4}$ s, and $\tau_F \approx 1.5 \times 10^{-3}$ s. Thus, $\tau_c \ll \tau_p < \tau_F$ which yields $\mathrm{Sa} \ll 1$ and $\mathrm{Re_E} \ll 1$ and we can assume the charge relaxation and charge convection to be negligible.

The electric field and the hydrodynamic fluid velocity are coupled at the drop interface through the stress balance

$$[\![\mathbf{T}^{\mathrm{H}} + \mathbf{T}^{\mathrm{E}}]\!] \cdot \boldsymbol{n} = -\nabla_{\mathrm{s}} \cdot \Sigma \tag{6}$$

where $\mathbf{T}^{\mathrm{H}} = -p\mathbf{I} + \mu[\nabla \boldsymbol{u} + (\nabla \boldsymbol{u})^{\mathrm{T}}]$ and $\mathbf{T}^{\mathrm{E}} = \varepsilon \boldsymbol{E}\boldsymbol{E} - \frac{\varepsilon}{2}(\boldsymbol{E} \cdot \boldsymbol{E})I$ are the viscous and electric stresses, Σ is given by a constitutive law that accounts for interfacial rheology. In this paper, we consider surface viscosities given *via* the Boussinesq–Scriven law:[57]

$$\Sigma = \gamma\mathbf{P} + (\lambda - \nu)\Theta\mathbf{P} + \nu\mathbf{D}^{\mathrm{s}}(\boldsymbol{u}_{\mathrm{s}}), \tag{7a}$$

$$\Theta = \nabla_{\mathrm{s}}\cdot\boldsymbol{u}_{\mathrm{s}}, \quad \mathbf{D}^{\mathrm{s}}(u_{\mathrm{s}}) = \nabla_{\mathrm{s}}\boldsymbol{u}_{\mathrm{s}} + (\nabla_{\mathrm{s}}\boldsymbol{u}_{\mathrm{s}})^{\mathrm{T}} \tag{7b}$$

where γ is the surface tension, $\mathbf{P} = \mathbf{I} - \boldsymbol{n}\boldsymbol{n}^{\mathrm{T}}$, Θ is the surface dilatation, $\mathbf{D}^{\mathrm{s}}(\boldsymbol{u}_{\mathrm{s}})$ is the surface deformation, λ, ν are parameters denoting the interface dilatational and shear viscosities, respectively. $\nabla_{\mathrm{s}} = \mathbf{P}\cdot\nabla$ is the surface divergence, and $\boldsymbol{u}_{\mathrm{s}} = \mathbf{P}\cdot\boldsymbol{u}$ is the surface velocity. Taking the surface divergence of eqn (7), the right-hand side of the stress balance eqn (6) becomes

$$[\![\mathbf{T}^{\mathrm{H}} + \mathbf{T}^{\mathrm{E}}]\!] \cdot \boldsymbol{n} = \kappa[\gamma + (\lambda - \nu)\Theta]\boldsymbol{n} - (\lambda - \nu)\nabla_{\mathrm{s}}\Theta \cdot \nu\mathbf{T}^{\mathrm{S}}, \tag{8a}$$

$$\mathbf{T}^{\mathrm{S}} = \nabla_{\mathrm{s}}\cdot\mathrm{D}^{\mathrm{s}}(\boldsymbol{u}_{\mathrm{s}}), \tag{8b}$$

where κ is the mean curvature.

2.2 Spheroidal model

In our formulation we focus on spheroidal deformations and seek a leading-order truncated solution in spheroidal coordinates as provided in ref. 28. The spheroidal coordinates system has been used successfully to analyze the electrohydrodynamics of leaky dielectric drops.[18,19,28,29,58–61] The reader is referred to these studies for detailed derivations. Here, we provide an outline of the solution.

Focusing on the axisymmetric flow, the prolate spheroidal coordinates (ξ,η) can be expressed in the cylindrical coordinates (r,z) as

$$z = c\xi\eta, \quad r = c\sqrt{(\xi^2 - 1)(1 - \eta^2)}, \tag{9}$$

where $c \equiv \sqrt{a^2 - b^2}$ is the semi-focal length, and a and b are the major and minor semi-axis, respectively. Defined as such, $\xi \in [1,\infty)$, $\eta \in [-1,1]$, and surfaces of constant ξ are spheroids while surfaces of constant η are hyperboloids. Therefore the prolate drop surface is simply *given* by $\xi = \xi_0(t) \equiv a/c$. Volume conservation of the drop relates a and b to $\xi_0(t)$ as $a(t) = r_0 \Big/ \sqrt[3]{1 - \xi_0(t)^{-2}}$ and $b(t) = r_0\sqrt[6]{1 - \xi_0(t)^{-2}}$, where r_0 is the radius of an initially spherical drop. In the following we use h_ξ, h_η and h_ζ to denote the metric coefficients in the prolate spheroidal coordinates.

The incompressible Stokes equations in eqn (1) are expressed in terms of the stream function that now satisfies the equation

$$(\boldsymbol{E}^2)^2\psi_j = 0, \tag{10}$$

where

$$\boldsymbol{E}^2 = \frac{1}{c(\xi^2 - \eta^2)}\left[(\xi^2 - 1)\frac{\partial^2}{\partial\xi^2} + (1 - \eta^2)\frac{\partial^2}{\partial\eta^2}\right].$$

Then, the flow field is calculated from $u_j = -\frac{1}{h_\xi h_\zeta}\frac{\partial\psi_j}{\partial\eta}$ and $v_j = \frac{1}{h_\eta h_\zeta}\frac{\partial\psi_j}{\partial\xi}$. The electric potentials ϕ_j in each phase are obtained from eqn (3) with the corresponding boundary conditions, and are then expressed in terms of Legendre functions. The flow field and electric potential problems are tied together at the drop interface through the stress balance. In the presence of surface rheology, the stress balance is modified to include the effects of surface shear and dilatational viscosities:

$$\left[\!\left[T^{\mathrm{H}}_{\xi\eta} + T^{\mathrm{E}}_{\xi\eta}\right]\!\right] = -(\lambda - \nu)H_{\eta\eta}\frac{\partial\Theta}{\partial\eta} - \nu T^{\mathrm{S}}_{\xi\eta}, \tag{11a}$$

$$\left[\!\left[T^{\mathrm{H}}_{\xi\xi} + T^{\mathrm{E}}_{\xi\xi}\right]\!\right] = \gamma\kappa + (\lambda - \nu)\kappa\Theta - \nu T^{\mathrm{S}}_{\xi\xi}, \tag{11b}$$

where

$$T^{\mathrm{S}}_{\xi\eta} = E_{\eta\zeta}H_{\zeta\zeta}D^{\mathrm{s}}_{\eta\eta} - E_{\eta\zeta}H_{\zeta\zeta}D^{\mathrm{s}}_{\zeta\zeta} + H_{\eta\eta}\frac{\partial D^{\mathrm{s}}_{\eta\eta}}{\partial\eta}, \tag{12a}$$

$$T^{\mathrm{S}}_{\xi\xi} = E_{\xi\eta}H_{\eta\eta}D^{\mathrm{s}}_{\eta\eta} + E_{\xi\zeta}H_{\zeta\zeta}D^{\mathrm{s}}_{\zeta\zeta}, \tag{12b}$$

$H_{\eta\eta} = 1/h_\eta$, $H_{\zeta\zeta} = 1/h_\zeta$, and $E_{ij} = \frac{1}{h_i}\frac{\partial h_j}{\partial x_i}$. The surface strain tensor D^{s} is provided in Appendix B. Taylor[62] first recognized the challenge of satisfying the stress balance over the surface of a spheroid. In our model, the solutions of the Stokes equation in prolate spheroidal coordinates are expressed as a series of Gegenbauer functions of the first and second kinds.[63,64] However, in our model we truncate the solutions and only keep the first mode.[19] As a result, the stress balance at this mode is not satisfied at every point on the spheroidal drop. To remedy this, we employ the approaches in ref. 58,65. We perform a Galerkin projection of the normal (tangential) stress balance onto the normal (tangential) velocity u (v), and integrate over the surface

$$\int_{\mathrm{S}} u \cdot \left[\left[T^{\mathrm{H}}_{\xi\eta} + T^{\mathrm{E}}_{\xi\eta}\right]\right] = -\int_{\mathrm{S}} u \cdot \left\{(\lambda - \nu) H_{\eta\eta} \frac{\partial \Theta}{\partial \eta} + \nu T^{S}_{\xi\eta}\right\}, \quad (13a)$$

$$\int_{\mathrm{S}} v \cdot \left[\left[T^{\mathrm{H}}_{\xi\xi} + T^{\mathrm{E}}_{\xi\xi}\right]\right] = \int_{\mathrm{S}} v \cdot \left\{\gamma\kappa + (\lambda - \nu)\kappa\Theta + \nu T^{\mathrm{S}}_{\xi\xi}\right\}. \quad (13b)$$

We non-dimensionalize the problem using r_0 for length, E_0 for electric field, $\varepsilon_2 {E_0}^2 r_0/\mu_1$ for velocity, and $\varepsilon_2 {E_0}^2$ for stresses. Three dimensionless parameters emerge from scaling: the electric capillary number $\mathrm{Ca_E} = \varepsilon_2 {E_0}^2 r_0/\gamma$, and the Boussinesq numbers $\mu_\mathrm{d} = \lambda/\mu_1 r_0$ and $\mu_\mathrm{s} = \nu/\mu_1 r_0$. However, the shear and dilatational viscosities may have, in exceptional cases, the same order of magnitude,[66,67] in general $\mu_\mathrm{d} \gg \mu_\mathrm{s}$.[68–72] For example, surface viscosity measurements for sodium lauryl sulfate (SLS; $\mu_\mathrm{d} \approx 2.5 \times 10^{-3}$ N s m^{-1}, $\mu_\mathrm{s} \approx 1.7 \times 10^{-7}$ N s m^{-1}) or sodium lauryl sulfate–lauryl alcohol (SLS–LOH; $\mu_\mathrm{d} \approx 39.8 \times 10^{-3}$ N s m^{-1}, $\mu_\mathrm{s} \approx 0.2 \times 10^{-3}$ N s m^{-1}).[73] In these cases, the dilatational viscosity is about 2 (SLS) to 4 (SLS–LOH) orders of magnitude larger than the shear viscosity ($\mu_\mathrm{d} \gg \mu_\mathrm{s}$). Considering a water–ethanol mm-sized drop with interior viscosity 0.042 N s^{-1} m^{-2},[8] the Boussinesq numbers would fall in the range $\approx 4 \times 10^{-3}$ to 9.5×10^2. In this study, we consider Boussinesq numbers ranging from 0 to 10^3.

After applying the approach in ref. 19 and 28, we can show that the solutions of the governing equations (together with the boundary conditions) reduce to an ordinary differential equation for the shape parameter

$$\frac{\mathrm{d}\xi}{\mathrm{d}t} = \frac{1}{\mathscr{F}}\left(\frac{\mathscr{Q}_\mathrm{T}}{c^2}\mathscr{H}_\mathrm{T} + \frac{\mathscr{Q}_\mathrm{N}}{c^2} f_{21} - f_{24}\right), \quad (14)$$

where

$$\mathscr{Q}_\mathrm{N} = \mathrm{Ca}_E\left[\left(-c + \alpha Q_1'\right)^2 + \left(-c + \alpha\frac{Q_1}{\xi_0}\right)^2 - 2\beta^2/\varepsilon_\mathrm{r}\right], \quad (15a)$$

$$\mathscr{Q}_T = \mathrm{Ca_E}\left[\left(-c + \alpha Q_1'\right)\left(-c\xi + \alpha Q_1\right) - \xi\beta^2/\varepsilon_\mathrm{r}\right], \quad (15b)$$

$$\mathscr{H}_\mathrm{T} = \frac{f_{11}\left(\mu_\mathrm{r} f_{22} + f_{23} - (\mu_\mathrm{d} - \mu_\mathrm{s}) f_{27} + \mu_\mathrm{s} f_{28}\right)}{\mu_\mathrm{r} f_{14} + f_{15} + (\mu_\mathrm{d} - \mu_\mathrm{s}) f_{16} + \mu_\mathrm{s} f_{17}}, \quad (15c)$$

$$\mathscr{F} = \frac{2}{3}\left(\mu_\mathrm{r} f_{25} + f_{26} - (\mu_\mathrm{d} - \mu_\mathrm{s}) f_{29} + \mu_\mathrm{s} f_{30}\right). \quad (15d)$$

In these equations, α, β are coefficients of the electric potential ϕ_j, Q_1 is a Gegenbauer function of the second kind,[63,64] and the primes denote differentiation with respect to ξ. The ξ-dependent functions f_n's are provided in Appendix A.

Moreover, in the absence of charge relaxation, contributions from the Maxwell stresses $\mathscr{Q}_\mathrm{N}/c^2$ and $\mathscr{Q}_\mathrm{T}/c^2$ reduce to

$$\mathscr{Q}_\mathrm{N}/c^2 = \mathrm{Ca_E} K^2\left(-2{\sigma_\mathrm{r}}^2/\varepsilon_\mathrm{r} + {\sigma_\mathrm{r}}^2 + 1\right), \quad (16a)$$

$$\mathscr{Q}_\mathrm{T}/c^2 = \mathrm{Ca_E} K^2 \sigma_\mathrm{r}(1 - \sigma_\mathrm{r}/\varepsilon_\mathrm{r}), \quad (16b)$$

where $K \equiv \left[Q_1(\xi_0) - \xi_0 Q_1'(\xi_0)\right]/\left[Q_1(\xi_0) - \sigma_\mathrm{r}\xi_0 Q_1'(\xi_0)\right]$.

3 Results and discussion

3.1 Model validation

Mandal and Chakraborty[47] performed an asymptotic analysis for a small electric capillary number $\mathrm{Ca_E} \ll 1$ to investigate the effects of surface viscosities on the dielectrophoresis of drops. A close inspection of their normal stress balance (eqn (15) in their paper) suggests that their small-deformation analysis is valid up to μ_s, $\mu_\mathrm{d} \sim \mathscr{O}(1)$. We use the small-deformation results to validate our spheroidal model predictions for the deformation number,

$$\mathscr{D} = \frac{a - b}{a + b}, \quad (17)$$

with the following expectations: (1) our results should agree qualitatively with their model for a fixed value of electric capillary number and varying μ_d, μ_s up to order 1; (2) our results should show good quantitative agreement with their model for a fixed value of the surface viscosities in the limit $\mathrm{Ca_E} \ll 1$.

Fig. 2 shows the deformation number for a phenylmethylsiloxane–dimethylsiloxane (PMM) drop suspended in silicone oil medium[47,74] with $\mu_\mathrm{r} = 1/1.4706$, $\sigma_\mathrm{r} = 1/1.25$, $\varepsilon_\mathrm{r} = 1/1.0566$ as a function of the surface viscosities (Fig. 2(a)) and as a function of the electric capillary number (Fig. 2(b)). The solid lines denote results from the large deformation analysis while the dashed lines represent results from the small deformation analysis in.[47] In Fig. 2(a), the electric capillary number is fixed at $\mathrm{Ca_E} = 0.2$. The curves are color-coded to denote the sole-effect of the dilatation viscosity (red), the sole-effect of the shear viscosity (blue), and their combined effect (black).

As expected, our spheroidal results show good qualitative agreement with the small deformation analysis for all three effects. Quantitatively, the difference between the two approximations is less than 1%. As previously predicted in ref. 47, the dilatation viscosity acts to increase the deformation whereas the shear viscosity suppresses it compared to a clean drop. In Fig. 2(b), the dilatational viscosity ($\mu_\mathrm{d} = 1$) and shear viscosity ($\mu_\mathrm{s} = 1$) are fixed, and the deformation is plotted as a function of the electric capillary number $\mathrm{Ca_E}$. The curves are color-coded to represent the sole-effect of the dilatation viscosity (red), the sole-effect of the shear viscosity (blue), and the clean drop case (black). For the given fluid properties, a strong electric field is necessary to yield significant drop deformation. At values of the electric capillary number up to ≈ 0.5, our results show excellent agreement with the predictions from the small deformation analysis. However, results from the small deformation analysis

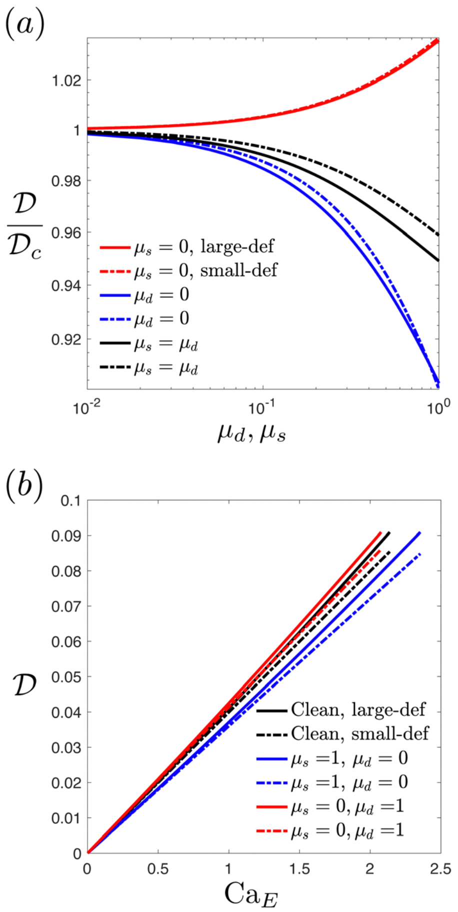

Fig. 2 (a) Equilibrium $\mathscr{D}$ deformation scaled by the clean drop deformation $\mathscr{D}_c$ as a function of the dilatational and shear viscosities for $\mathrm{Ca_E} = 0.2$. The curves are color-coded to denote the sole-effect of dilatational viscosity (red), shear viscosity (blue) and their combined effect (black). (b) Equilibrium deformation $\mathscr{D}$ as a function of electric capillary number. The curves are color-coded to denote the sole-effect of dilatational viscosity (red), shear viscosity (blue) and the clean drop case (black). In both panels, the solid curves represent results from the large deformation analysis (large-def) and the dashed curves represent results from the small-deformation analysis (small-def) in ref. 47. Other parameters are $\mu_r = 1/1.4706$, $\sigma_r = 1/1.25$, $\varepsilon_r = 1/1.0566$.

become less accurate and consequently deviate from the large deformation analysis results at a stronger electric field and larger $\mathscr{D}$. Contrasting Fig. 2(b) and 3(a), we note that Fig. 2(b) remains in the small deformation regime ($\mathscr{D} < 0.1$) for a large range of $\mathrm{Ca_E}$. This is not true for Fig. 3(a), where $0 < \mathscr{D} < 0.3$. Zooming into $0 < \mathscr{D} < 0.1$ (the small deformation regime) in Fig. 3(a) reveals that the deformation is of a similar magnitude compared to Fig. 2(b).

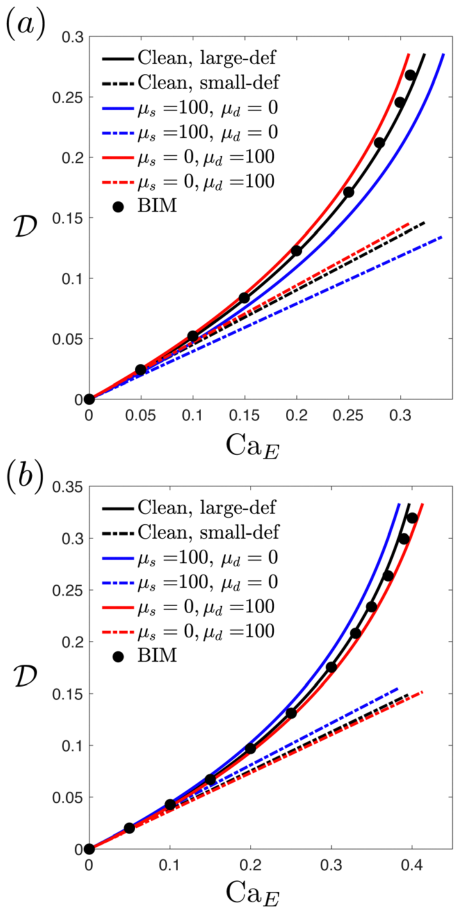

Fig. 3 Equilibrium deformation $\mathscr{D}$ as a function of the electric capillary number for (a) a prolate 'A' drop with $\mu_r = 1$, $\sigma_r = 0.1$, $\varepsilon_r = 10$ and (b) a prolate 'B' drop with $\mu_r = 1$, $\sigma_r = 0.04$, $\varepsilon_r = 1/50$. In (a) and (b), the solid curves represent results from the large deformation analysis (large-def), the dashed curves represent results from the small deformation analysis (small-def) in ref. 47, and the symbols denote boundary integral method simulations for a clean drop.[12] In both panels, the curves are color-coded to denote the sole-effect of dilatational viscosity (red), shear viscosity (blue) and the clean drop case (black).

3.2 Effect of surface viscosities on deformation

3.2.1 Influence of interior circulation. A leaky dielectric drop in a leaky dielectric medium can deform into a prolate or oblate shape, depending on the fluids' electric parameters.[5–7,12] Moreover, as illustrated in Fig. 1(b) two modes of deformation exist for a prolate drop: the prolate 'A' drop with an equator-to-pole circulation, and the prolate 'B' drop with a pole-to-equator circulation. In this section, we investigate the effects of varying the surface viscosities on the deformation for a wider range of electric capillary numbers.

Fig. 3 shows the deformation number as a function of the electric capillary number for a drop with equator-to-pole circulation ((Fig. 1(a), $\mu_r = 1$, $\sigma_r = 0.1$, $\varepsilon_r = 10$, prolate 'A') and with pole-to-equator circulation (Fig. 1(b), $\mu_r = 1$, $\sigma_r = 0.04$, $\varepsilon_r = 1/50$, prolate 'B'). For these electric parameters, numerical simulations[12] reveal a critical electric capillary number (the value beyond which equilibrium deformations cease to exist).

For the clean drops, the boundary integral method simulations[12] agree well with our spheroidal model[19,28] for the full range of electric capillary numbers. By comparison, the small deformation theory (dashed curves) shows agreement only up to $\mathrm{Ca_E} \approx 0.1$.

Surface rheology affects the deformation in several important ways. First, the effects of the shear viscosity ($\mu_s = 100$, blue curves) appears to be more significant than those from the dilatation viscosity (μ_d = 100, red curves). This is observed by the larger magnitude of deformation compared to the clean drop, and is especially pronounced for a prolate 'A' drop (Fig. 2(b) and 3(a)). Second, the rheological effects depend on circulation. Indeed, the dilatation viscosity yields larger (smaller) deformation compared to the clean drop when the interior circulation is from equator-to-pole (pole-to-equator). The reverse is true for the shear viscosity: smaller (larger) deformation is predicted for a prolate 'A' (prolate 'B') drop. Third, Fig. 3(a) and (b) also suggest some effects on the critical electric capillary number, beyond which equilibrium shapes cannot be achieved and the drop breaks up. Since dilatational viscosity yields larger deformation compared to the clean drop, it suggests that the critical electric capillary number is reduced. Likewise, the critical electric capillary number is increased as a result of shear viscosity. In other words: the dilatation (shear) viscosity destabilizes (stabilizes) the drop. This is consistent with recent results for a settling drop under gravity.[41]

3.2.2 Combined effect of surface viscosities. We observe from Fig. 2(a) that deformation can be enhanced or suppressed depending on various combinations of the surface viscosities. Fig. 4 shows a phase plane for the combined effect of the shear and dilatational viscosities on the equilibrium deformation of a prolate 'A' drop (Fig. 4(a)) and prolate 'B' drop (Fig. 4(b)). In both panels, the electric capillary number $\mathrm{Ca_E}$ = 0.2, and the deformation $\mathscr{D}$ is scaled by the clean drop deformation $\mathscr{D}_c$.

For a given prolate mode ('A' or 'B'), the figure shows regions where the combination yields deformation that is larger ($\mathscr{D}/\mathscr{D}_c > 1$) or smaller ($\mathscr{D}/\mathscr{D}_c < 1$) compared to the clean drop case. Our results show that the boundaries between the two regions are the lines $\mu_s = \mu_d/2.68$ (prolate 'A') and $\mu_s = \mu_d/2.64$ (prolate 'B'). In the case of the prolate 'A' drop, surface rheology yields larger deformation when $\mu_s < \mu_d/2.68$, and smaller deformation otherwise. For the prolate 'B' drop, larger (or smaller) deformation is attained for $\mu_s > \mu_d/2.64$ (or $\mu_s < \mu_d/2.64$).

The deformation $\mathscr{D} = \mathscr{D}_c$ when the surface viscosities combine in such a way to balance surface dilatation with surface deformation in eqn (11b):

$$\mu_d\kappa\Theta \sim \mu_s(\kappa\Theta - T^{S}_{\xi\xi}). \tag{18}$$

Fig. 5(a) (prolate 'A') and Fig. 5(b) (prolate 'B') illustrate this balance that yields identical deformations between drops with

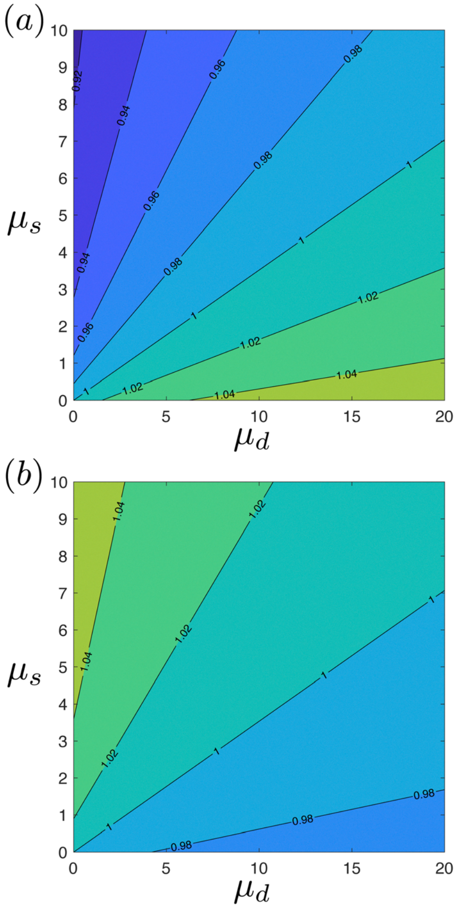

Fig. 4 Deformation phase plane for (a) the prolate 'A' and (b) prolate 'B' drops in Fig. 3(a) and (b). The contour line $\mathscr{D}/\mathscr{D}_c = 1$ denote the boundary between regions of higher and lower deformations compared to the clean drop. The electric capillary number $\mathrm{Ca_E}$ = 0.2.

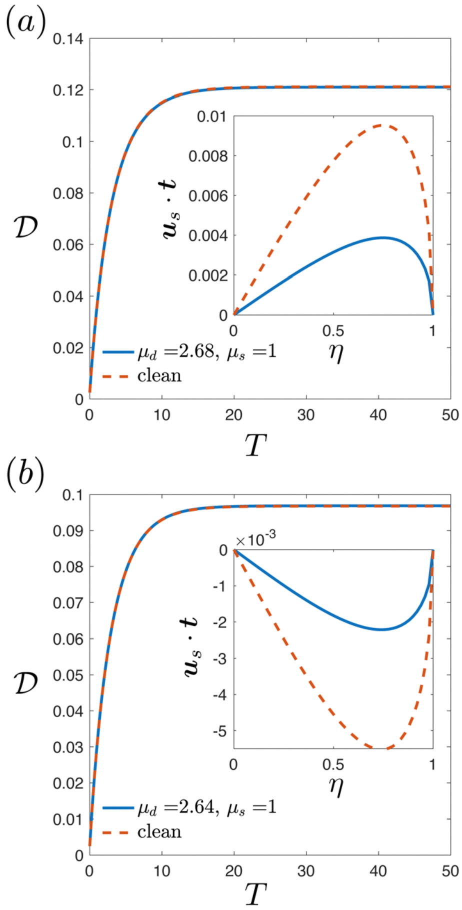

Fig. 5 Deformation number as a function of dimensionless time for (a) the prolate 'A' and (b) prolate 'B' drops in Fig. 3(a) and (b). The dashed and solid lines denote the clean and surface viscosities influenced drops, respectively. The insets show the tangential component of the surface velocity as a function of the drop surface parameter η. The electric capillary number $\mathrm{Ca_E}$ = 0.2.

interfacial viscosities and clean drops. The insets in Fig. 5(a) and (b) show the tangential surface velocity, where the flow is suppressed due to surface rheology. The combination of surface viscosities yields the clean drop deformation despite the reduction in flow that results from viscous damping on the surface. The decrease in flow is consistent with previous studies that showed that the effect of dilatational viscosity or shear viscosity is to reduce the flow in and around the drop.[34] More extensive predictions from our model (see Appendix C) also verified that surface viscosities completely suppress the surface flow and, by extension, the flow in and around the drop in the limit $\mu_{\mathrm{d}}, \mu_{\mathrm{s}} \to \infty$. In these cases the drop becomes immobilized since the flow vanishes (viscous stress is zero), and the drop can no longer deform (the normal Maxwell stress balances out surface tension force). Moreover, for a given electric capillary number $\mathrm{Ca_E}$ and set of electric parameters (σ_{r},ε_{r}), the critical ratio $\alpha \equiv \mu_{\mathrm{d}}/\mu_{\mathrm{s}}$ that results in $\mathscr{D} = \mathscr{D}_{\mathrm{c}}$ can be approximated from eqn (18) (see Appendix D). Our analysis shows that it is the result of competing, and opposing, actions between surface dilatation and surface deformation.

3.2.3 Influence of surface viscosities on conducting drops.

In previous sections, we focused on the effects of surface rheology on leaky dielectric drops. It is natural to ponder whether surface viscosities would affect conducting drops in similar fashion. To investigate this inquiry, we use experimental data for a water–ethanol droplet in silicone oil[8] with $\mu_{\mathrm{r}} = 23.3$, $\sigma_{\mathrm{r}} = 10^{-5}$, $\varepsilon_{\mathrm{r}} = 0.05$ and examine the dynamics at equilibrium and above the critical electric capillary number.

At equilibrium: for a conducting drop, the tangential electric stress $\mathscr{Q}_{\mathrm{T}}/c^2 \approx 0$. Thus, the product $\mathscr{Q}_{\mathrm{T}}\mathscr{H}_{\mathrm{T}}/c^2 \approx 0$ in eqn (14) and the equilibrium deformation is solely the result of the balance between the normal electric stress and the surface tension force. Since the surface viscosities enter the dynamics through $\mathscr{H}_T$, we expect the equilibrium deformation to be independent of surface rheology. Fig. 6(a) shows the aspect ratio *a*/*b* as a function of dimensional time with $\mathrm{Ca_E} = 0.2$. The curves resulting from the presence of dilatational and shear viscosities are identical to the clean drop case at equilibrium, consistent with our analysis of eqn (14). The inset in the figure focuses on the region, around $T = 0.5$ s, with the largest difference between the curves. It shows that, while surface rheology has no effects on the equilibrium deformation, it does affect the transient deformation. Again, this is expected from the expression of $\mathscr{F}$ in eqn (14). We note that for the case of dilatational viscosity, our result is consistent with a recent study that showed that the dilatational viscosity has no effect on the equilibrium deformation of a conducting drop.[48] Based on our analysis, the study's conclusion extends to shear viscosity as well.

Above the critical electric capillary number: Fig. 6(b) shows the experimental data and predictions from the large deformation analysis for the aspect ratio *a*/*b* as a function of dimensional time. The symbols represent the experimental data, with an estimated 10% fitting error (error bars). The aspect ratio slowly rises before a drastic jump. Given similar fluids' electric parameters, the onset of the jump occurs around $t \approx 9$ s. Surface viscosities, μ_{d} and μ_{s} lead to an earlier jump onset compared to the clean drop case. The time of the onset in this case depends on the magnitude of the surface viscosities. In the case of an inviscid drop ($\mu_{\mathrm{r}} \to \infty$), we expect all three transient shapes to be nearly identical since the effects of surface rheology depend on the viscosity contrast, with inviscid droplets being affected most by the interfacial rheology.[34]

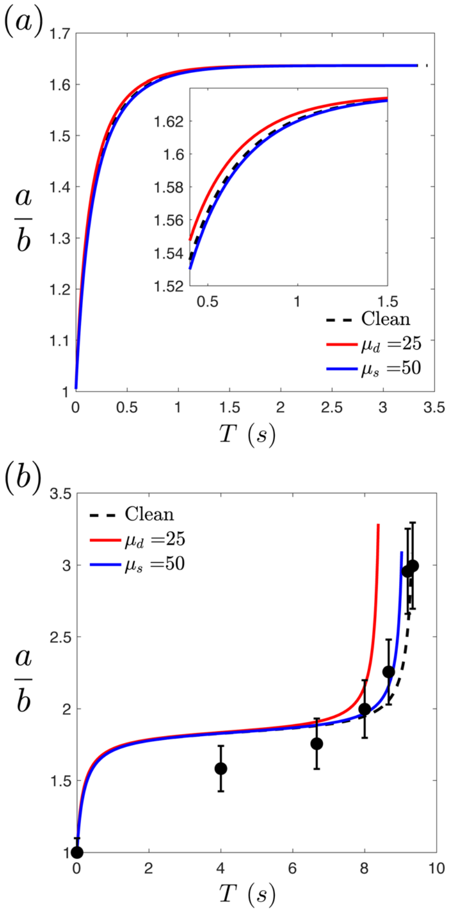

Fig. 6 The aspect ratio *a*/*b* as a function of dimensional time *t* for $\mu_{\mathrm{r}} = 23.3$, $\sigma_{\mathrm{r}} = 10^{-5}$, $\varepsilon_{\mathrm{r}} = 0.05$. The electric capillary number (a) $\mathrm{Ca_E} = 0.2$ and (b) $\mathrm{Ca_E} = 0.20469$. In both panels, the curves are color-coded to denote the sole-effect of dilatational viscosity (red), shear viscosity (blue), and the clean drop case (black). The symbols in (b) represent experimental results for the clean drops including a 10% fitting error (error bars).[8]

3.3 Magnitude of drop deformation depends on interplay between surface dilatation and surface deformation

The surface shear and dilatational viscosities both act to reduce the drop surface velocity $\boldsymbol{u}_{\mathrm{s}}$, which may be entirely suppressed as $\mu_{\mathrm{d}}, \mu_{\mathrm{s}} \to \infty$. Since both surface viscosities reduce the surface velocity, the latter alone is not sufficient to understand the opposite effect of the dilatational and shear viscosities on the deformation. Moreover, we recall that the effect of surface rheology also depends on the drop's interior circulation (pole-to-equator or equator-to-pole). To further understand this deformation dynamic, we recast the normal stress balance equation as

$$\underbrace{[\![T^{\mathrm{H}}_{\xi\xi}]\!]}_{\Delta_1} + \underbrace{[\![T^{\mathrm{E}}_{\xi\xi}]\!]}_{\Delta_2} - \underbrace{\mu_{\mathrm{d}}\kappa\Theta}_{\Delta_3} - \underbrace{\mu_{\mathrm{s}}\left(T^{\mathrm{S}}_{\xi\xi} - \kappa\Theta\right)}_{\Delta_4} = \underbrace{\gamma\kappa}_{\Delta_5}. \qquad (19)$$

In the presence of surface viscosities, eqn (19) shows that equilibrium drop deformations depend on nontrivial interplay between viscous (Δ_1), electric (Δ_2), and surface stresses (Δ_3–Δ_5). In the next sections, we investigate the surface dilatation and surface deformation for the two prolate modes separately, and we also analyze these surface variables to extract useful insights into the stability of the drop. To address the surface rheology effects simultaneously we consider combinations of surface viscosities such that $\mathscr{D}/\mathscr{D}_c > 1$ and $\mathscr{D}/\mathscr{D}_c < 1$ from Fig. 4.

3.3.1 Equilibrium prolate 'A' shape. As a representative case, we consider the prolate 'A' drop with $\mu_r = 1$, $\sigma_r = 0.1$, $\varepsilon_r = 10$. Fig. 7 shows the dimensionless number (a), surface dilatation, $\Theta = \nabla_s \cdot \boldsymbol{u}_s$ (b), and surface deformation (c) when $\mathscr{D}/\mathscr{D}_c > 1$. As we noted earlier, the sole-effect of the dilatational viscosity ($\mu_s = 0$) on a prolate 'A' drop is to increase deformation compared to the clean drop case. In this case, the normal stress balance reduces to $\Delta_1 + \Delta_2 - \Delta_3 = \Delta_5$. Since $\Theta < 0$ at the poles, the term $-\Delta_3$ is positive and thus the drop expands at the pole, which results in an increase in the curvature and larger deformation compared to the clean drop.

Surface deformation (Δ_4) begins to play a role when the shear viscosity is introduced. For $\mu_d = 10, \mu_s = 1$ [Fig. 7(a)–(c)], $-\Delta_4$ is negative; however, the net result $-\Delta_3 - \Delta_4 > 0$. The combination of the surface viscosities yields a larger curvature at the poles, resulting in a larger deformation compared to the clean drop (Fig. 7(a)). On the other hand, when $\mu_d = 1, \mu_s = 10$ [Fig. 7(d)–(f)], the net result $-\Delta_3 - \Delta_4 < 0$. In this case, the curvature of the drop must decrease in order to balance eqn (19). The reduction in curvature in turn leads to smaller deformation compared to the clean drop case (Fig. 7(d)).

It is worth noting that a larger shear viscosity increases the viscous damping that acts to suppress the flow. Changes in the flow in turn have a direct effect on the deformation: a larger deformation is expected when μ_s is low (Fig. 7) *versus* when the shear viscosity is high (Fig. 7(d)). The increase and decrease in deformation compared to the clean drop case is illustrated in Fig. 9(a) along with the streamlines. The dashed curves represent the clean drop. Here we note that the flow is more suppressed when $\mathscr{D}/\mathscr{D}_c < 1$ (left-half of Fig. 9(a)). This dynamics contrasts with the stronger circulation we observe for $\mathscr{D}/\mathscr{D}_c > 1$ (right-half of Fig. 9(a)).

3.3.2 Equilibrium prolate 'B' shape. We consider the prolate drop with $\mu_r = 1$, $\sigma_r = 0.04$, $\varepsilon_r = 1/50$, and begin by analyzing the rheological effect in the absence of dilatational viscosity. The normal stress balance reduces to $\Delta_1 + \Delta_2 - \Delta_4 = \Delta_5$, and both the surface dilatation and surface deformation play a role. However, the surface deformation dominates over surface dilatation. The term $-\Delta_4 > 0$, resulting in an increase in the curvature at the poles and a larger deformation compared to the clean drop case.

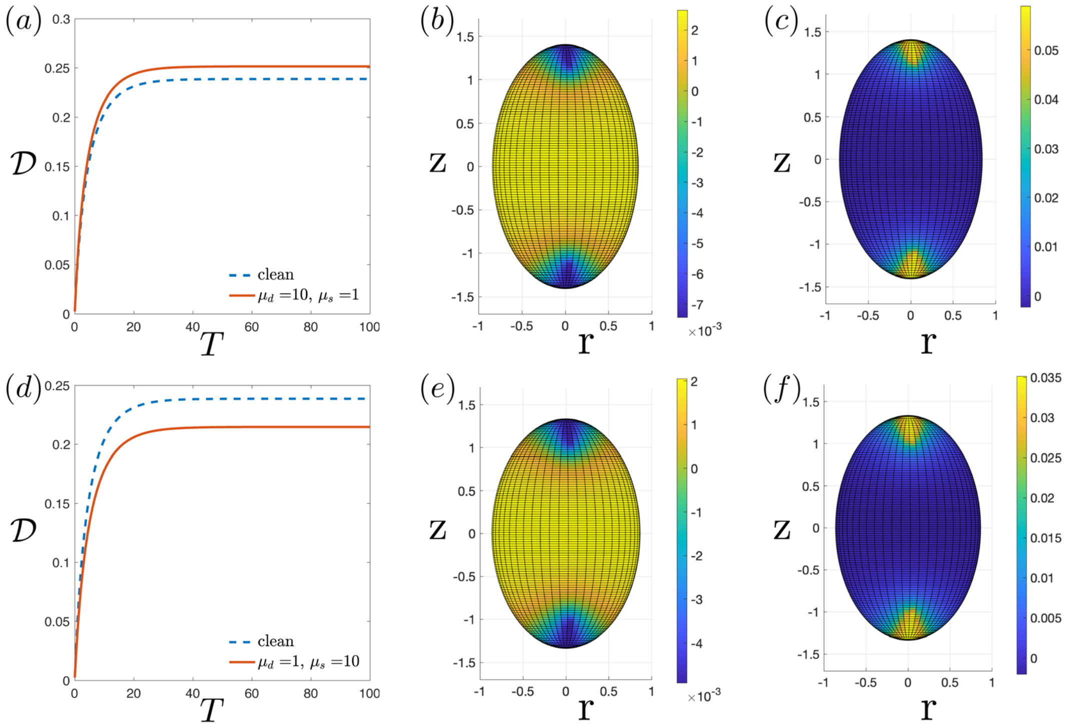

Fig. 7 (a and d) Deformation as a function of dimensionless time; (b and e) surface dilatation, $\Theta = \nabla_s \cdot \boldsymbol{u}_s$, and (c and f) surface deformation, $T^{\mathrm{S}}_{\xi\xi}$ for the prolate 'A' drop in Fig. 3(a). The top row represents the case with $\mu_d = 10$, $\mu_s = 1$ ($\mathscr{D}/\mathscr{D}_c > 1$), and the bottom row represents the case with $\mu_d = 1$, $\mu_s = 10$ ($\mathscr{D}/\mathscr{D}_c < 1$). The colormaps show the magnitude and distribution of the surface dilatation and surface deformation. The electric capillary number $\mathrm{Ca_E} = 0.3$, and the surface dilatation and surface deformation correspond to $T = 100$.

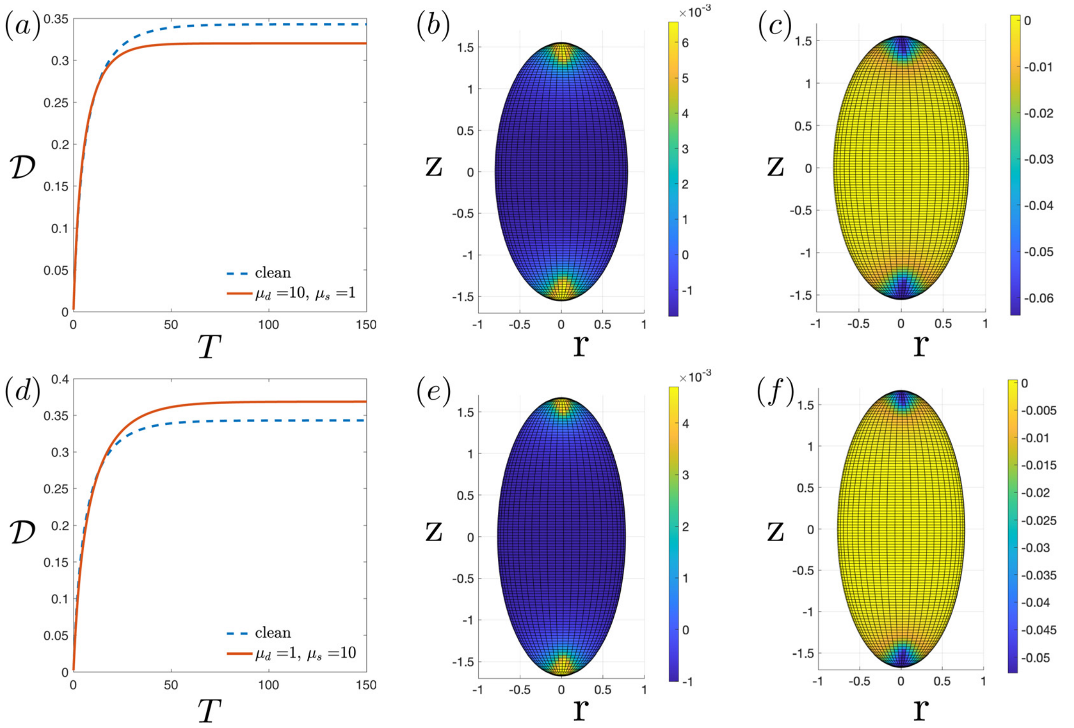

Fig. 8 (a and d) Deformation as a function of dimensionless time; (b and e) surface dilatation, $\Theta = \nabla_s \cdot \boldsymbol{u}_s$, and (c and f) surface deformation, $T^S_{\xi\xi}$ for the prolate 'B' drop in Fig. 3(b). The top row represents the case with $\mu_d = 10$, $\mu_s = 1$ ($\mathscr{D}/\mathscr{D}_c < 1$), and the bottom row represents the case with $\mu_d = 1$, $\mu_s = 10$ ($\mathscr{D}/\mathscr{D}_c > 1$). The colormaps show the magnitude and distribution of the surface dilatation and surface deformation. The electric capillary number $\mathrm{Ca_E}$ = 0.4, and the surface dilatation and surface deformation correspond to T = 150.

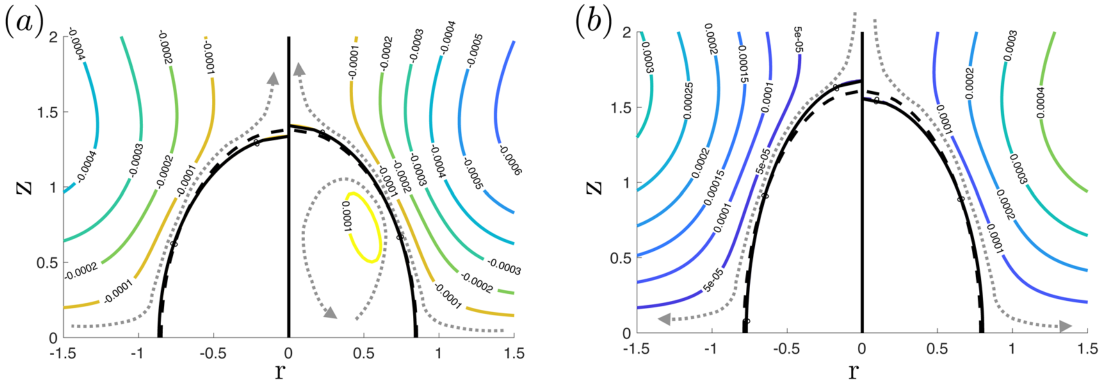

Fig. 9 Drop shapes and streamlines (a) for the prolate 'A' drop in Fig. 3(a) with $\mathrm{Ca_E}$ = 0.3, and (b) for the prolate 'B' drop in Fig. 3(b) with $\mathrm{Ca_E}$ = 0.4. In each panel, the left-half shows the shape with $\mu_s = 10$, $\mu_d = 1$, and the right-half shows the shape with $\mu_s = 1$, $\mu_d = 10$. In both panels, the dashed curve denotes the clean drop shape. Numbers on the streamline denote the magnitude of the flow, while the dotted lines show the direction of the flow.

Gradually increasing the dilatational viscosity leads to an even greater influence of surface dilatation (Δ_3). At low values of the dilatational viscosity [Fig. 8(d)–(f)], the contribution of Δ_4 still dominates, and the corresponding combinations of surface viscosities also yield larger deformation (Fig. 8(d)). On the other hand, when $\mu_d = 10, \mu_s = 1$ [Fig. 8(a)–(c)], the balance between surface dilatation and surface deformation is reversed. The surface dilatation now dominates and the net result $-\Delta_3 - \Delta_4 < 0$. Correspondingly, the combinations of surface viscosities yield a smaller deformation compared to the clean drop case (Fig. 8(a)).

We also illustrate the drop shape and circulation for the prolate 'B' drop in Fig. 9(b). For this prolate mode with a pole-to-equator circulation, a larger deformation is expected when μ_s is high [Fig. 8(d) and 9(b) (left-half)] *versus* when the shear viscosity is low [Fig. 8(a) and 9(b) (right-half)].

4 Conclusions

We investigated the effects of surface rheology on the electrohydrodynamics of a viscous drop by considering various modes of prolate deformation. We solved the governing equations by performing a large deformation analysis based on spheroidal harmonics. The model is validated against a previous study based on small-deformation analysis ($\mathrm{Ca_E} \ll 1$),[47] and is found to be in good agreement with the previous results in the literature.

We then use our model to investigate a range of surface rheological effects on deformation. We found that the influence of surface viscosities varies with (i) the fluids' electric parameters that determine the circulation and type of drops (leaky *versus* conducting), and (ii) the viscosity contrast. The main findings are summarized as follows:

- While the effects of surface viscosities on the deformation of the prolate 'A' drop are consistent with observations from previous studies,[39] the prolate 'B' reveals patterns not previously reported: shear (dilatational) viscosity enhances (suppresses) deformation (this finding highlights the importance of flow direction in assessing surface viscosity effects).
- For a given prolate mode ('A' or 'B'), surface viscosities can be combined to affect the strength of the flow, resulting in deformations that are larger (low viscous damping) or smaller (high viscous damping) compared to the clean drop case.
- Surface viscosities affect the critical electric capillary number, consistent with previous studies.[41,43] For an unstable drop, both surface viscosities together speed up the onset of blow up (the time when the rate of drop break up is the highest).
- As μ_d, $\mu_s \to \infty$ the flow is completely suppressed and the drop becomes immobilized (see Appendix C).

To explain the various observations, we analyzed surface deformation and surface dilatation which play important roles when surface viscosities are accounted for. We determined that the nontrivial influence of surface viscosities on drop deformation are a result of the interplay between dilatation and surface deformation. Our results can also be understood by considering a dilatational viscosity-induced effective surface tension $\gamma_{\mathrm{eff}} = \gamma - \mu_d\Theta$. For a prolate 'A' drop, the average surface dilatation is positive, leading to a reduction in surface tension ($\gamma_{\mathrm{eff}} < \gamma$) and thus an increase in deformation. For a prolate 'B' drop, the average surface dilatation is negative, yielding $\gamma_{\mathrm{eff}} > \gamma$) and a decrease in deformation. Moreover, we confirmed previous results that surface rheology does not affect the equilibrium deformation of a conducting drop.[48]

The effects of surface viscosities are not easily measured experimentally. Our findings, together with flow and deformation data, provide another tool for approximating the effects and/or values of the surface viscosities. Moreover, the rich dynamics of behaviors we discussed suggests that the flow and deformation can be effectively controlled by optimizing surface viscosities.

In our previous work,[29] we found the equilibrium deformations of some surfactants-covered drops to be $\mathscr{D} = 0.4$ (prolate 'A', $\sigma_r = 1/3, \varepsilon_r = 1$) and $\mathscr{D} = 0.05$ (prolate 'B', $\sigma_r = 1/3, \varepsilon_r = 1/3.5$) with surfactants coverage $\chi = 0.3$, surface Péclet number $\mathrm{Pe_s} = 10$ and $\mathrm{Ca_E} = 1$. These deformations are of the same order of magnitude as those obtained using the rheological model in the present study (for the prolate 'A' drop, $\mathscr{D} > 0.4$ with $\mu_d = 100$ and $\mathscr{D} \approx 0.37$ with $\mu_s = 100$, while for the prolate 'B' drop, $\mathscr{D} \approx 0.047$ with $\mu_d = 100$ and $\mathscr{D} > 0.05$ with $\mu_s = 100$). This comparison suggests that both Marangoni and surface viscosities effects are important, and a complete picture of the effects of surfactants on drops in a dc electric field must include both effects. We are currently working on incorporating Marangoni stress into our model and will expand on these results in future studies.

Conflicts of interest

There are no conflicts to declare.

Appendices

Appendix A. Shape dependent functions

The functions $f_{11}(\xi_0) - f_{17}(\xi_0)$ in eqn (14), (15c) and (15d) are given as follows:

$$f_{11} = \int \frac{\eta G_3(\eta)}{\xi_0^2 - \eta^2} \mathrm{d}\eta, \tag{20}$$

$$f_{12} = \frac{1}{\xi_0^2 - 1} \int G_3(\eta) \left(\frac{2\eta G_3'(\eta)}{(\xi_0^2 - \eta^2)^2} + \frac{G_3''(\eta)}{\xi_0^2 - \eta^2} \right) \mathrm{d}\eta, \tag{21}$$

$$f_{13} = \frac{G_3' G_5'' - G_5' G_3''}{2N} f_{11}, \tag{22}$$

$$f_{14} = -\xi_0 H_3' \int \frac{\eta G_3(\eta)}{(\xi_0^2 - \eta^2)^2} \mathrm{d}\eta + \frac{H_3''}{2} f_{11}, \tag{23}$$

$$f_{15} = \xi_0 H_3' \int \frac{\eta G_3(\eta)}{(\xi_0^2 - \eta^2)^2} \mathrm{d}\eta - \frac{\left(G_3 G_5'' - G_5 G_3''\right) H_3'}{2N} f_{11}, \tag{24}$$

$$f_{16} = \frac{\xi_0^2 \sqrt{\xi_0^2 - 1} H_3'}{c} \int \frac{\eta^2 \left(\eta^2 - 1\right)}{\left(\xi_0^2 - \eta^2\right)^{7/2}}, \tag{25}$$

$$f_{17} = \frac{\xi_0^2 H_3'}{2c\sqrt{\xi_0^2 - 1}} \int \frac{\eta^2 \left(\eta^2 - 5\xi_0^2 + 4\right)\left(1 - \eta^2\right)}{\left(\xi_0^2 - \eta^2\right)^{7/2}}, \tag{26}$$

The functions $f_{21}(\xi_0) - f_{29}(\xi_0)$, and $f_{30}(\xi_0)$ in eqn (14), (15c), and (15d) are given as follows:

$$f_{21} = \frac{\xi_0^2}{2} \int \frac{\left(3\eta^2 - 1\right)\left(\eta^2 - 1\right)}{\xi_0^2 - \eta^2} \mathrm{d}\eta, \tag{27}$$

$$\begin{aligned} f_{22} = {} & -H_3' \int \frac{\left(1 - 3\eta^2\right)\left(2\eta^4 + \xi_0^2 - 3\xi_0^2\eta^2\right)}{\left(\xi_0^2 - \eta^2\right)^2} \mathrm{d}\eta \\ & + 3H_3\xi_0 \int \frac{1 - 3\eta^2}{\xi_0^2 - \eta^2} \mathrm{d}\eta, \end{aligned} \tag{28}$$

$$f_{23} = -\frac{49}{30N}G_3H_3'\left(1-3{\xi_0}^2\right) + H_3'\int\frac{\left(1-3\eta^2\right)\left(2\eta^4+{\xi_0}^2-3{\xi_0}^2\eta^2\right)}{\left({\xi_0}^2-\eta^2\right)^2}\mathrm{d}\eta, \tag{29}$$

$$f_{24} = \frac{1}{c}\left[\xi_0\left({\xi_0}^2-1\right)^{1/2}\int\frac{3\eta^2-1}{\left({\xi_0}^2-\eta^2\right)^{3/2}}\mathrm{d}\eta + \frac{\xi_0}{\left({\xi_0}^2-1\right)^{1/2}}\int\frac{3\eta^2-1}{\left({\xi_0}^2-\eta^2\right)^{1/2}}\mathrm{d}\eta,\right. \tag{30}$$

$$\begin{aligned} f_{25} = &-\frac{\xi_0}{{\xi_0}^2-1}\int\frac{\left(1-3\eta^2\right)\left(2{\xi_0}^2-\eta^2-1\right)G_3'(\eta)}{\left({\xi_0}^2-\eta^2\right)^2}\mathrm{d}\eta \\ &+3\xi_0\int\frac{1-3\eta^2}{{\xi_0}^2-\eta^2}\mathrm{d}\eta \\ &+\frac{(\mu_\mathrm{r}-1)f_{12}+f_{13}}{\mu_\mathrm{r}f_{14}+f_{15}+(\mu_\mathrm{d}-\mu_\mathrm{s})f_{16}+\mu_\mathrm{s}f_{17}} \\ &\times\left(H_3'\int\frac{\left(1-3\eta^2\right)\left(2\eta^4+\xi_0^2-3{\xi_0}^2\eta^2\right)}{\left({\xi_0}^2-\eta^2\right)^2}\mathrm{d}\eta\right. \\ &\left.-3\xi_0H_3\int\frac{1-3\eta^2}{{\xi_0}^2-\eta^2}\mathrm{d}\eta\right), \end{aligned} \tag{31}$$

$$\begin{aligned} f_{26} = &\frac{\xi_0}{{\xi_0}^2-1}\int\frac{\left(1-3\eta^2\right)\left(2{\xi_0}^2-\eta^2-1\right)G_3'(\eta)}{\left({\xi_0}^2-\eta^2\right)^2}\mathrm{d}\eta - \frac{49}{30N}\left(1-3{\xi_0}^2\right)G_3' \\ &+\frac{(\mu_\mathrm{r}-1)f_{12}+f_{13}}{\mu_\mathrm{r}f_{14}+f_{15}+(\mu_\mathrm{d}-\mu_\mathrm{s})f_{16}+\mu_\mathrm{s}f_{17}} \\ &\times\left(-H_3'\int\frac{\left(1-3\eta^2\right)\left(2\eta^4+{\xi_0}^2-3{\xi_0}^2\eta^2\right)}{\left({\xi_0}^2-\eta^2\right)^2}\mathrm{d}\eta\right. \\ &\left.+\frac{49}{30N}G_3H_3'\left(1-3{\xi_0}^2\right)\right), \end{aligned} \tag{32}$$

$$f_{27} = \frac{{\xi_0}^{4/3}H_{3'}}{\left({\xi_0}^2-1\right)^{1/6}}\int\frac{\left(1-3\eta^2\right)\left(2{\xi_0}^2-\eta^2-1\right)\left(\eta^4+{\xi_0}^2\left(1-2\eta^2\right)\right)}{\left({\xi_0}^2-\eta^2\right)^{7/2}}, \tag{33}$$

$$\begin{aligned} f_{28} = &\frac{\xi_0H_3'}{c\sqrt{{\xi_0}^2-1}}\int\frac{\left(1-3\eta^2\right)}{\left({\xi_0}^2-\eta^2\right)^{7/2}} \\ &\times\left(\eta^4+\eta^6-{\xi_0}^4\left(1-3\eta^2\right)-{\xi_0}^2\left(3\eta^4+2\eta^2-1\right)\right) \end{aligned} \tag{34}$$

$$f_{29} = \frac{(\mu_\mathrm{r}-1)f_{12}+f_{13}}{\mu_\mathrm{r}f_{14}+f_{15}+(\mu_\mathrm{d}-\mu_\mathrm{s})f_{16}+\mu_\mathrm{s}f_{17}}f_{27}, \tag{35}$$

$$f_{30} = \frac{(\mu_\mathrm{r}-1)f_{12}+f_{13}}{\mu_\mathrm{r}f_{14}+f_{15}+(\mu_\mathrm{d}-\mu_\mathrm{s})f_{16}+\mu_\mathrm{s}f_{17}}f_{28}. \tag{36}$$

Unless otherwise defined, the Gegenbauer functions $G_n \equiv G_n(\xi_0)$ and $H_3 \equiv H_3(\xi_0)$.

Appendix B. Derivation of differential operators and surface variables in prolate spheroidal coordinates

We consider the prolate spheroidal coordinates (ξ, η, ζ) and, as a first step, we assume the problems to be axisymmetric $(\partial/\partial\zeta = 0, u_\zeta = 0)$. The unit normal vector $\boldsymbol{n} = \boldsymbol{e}_\xi = (1,0,0)$.

B.1 Surface rate of the strain tensor

The components of the projection tensor $\mathbf{P} = \mathbf{I} - \boldsymbol{nn}^\mathrm{T}$ in prolate spheroidal coordinates (PSC) are

$$\mathbf{P} = P_{ij}\boldsymbol{e}_i\boldsymbol{e}_j = \begin{pmatrix} 0 & 0 & 0 \\ 0 & 1 & 0 \\ 0 & 0 & 1 \end{pmatrix} \tag{37}$$

For the axi-symmetric problem, the strain tensor

$$\mathbf{D}(\mathbf{u}) = \begin{pmatrix} D_{\xi\xi} & D_{\xi\eta} & 0 \\ D_{\eta\xi} & D_{\eta\eta} & 0 \\ 0 & 0 & D_{\zeta\zeta} \end{pmatrix} \tag{38}$$

where

$$D_{\xi\xi} = 2\frac{(\partial v/\partial\xi)\sqrt{\xi^2-1}\left(\xi^2-\eta^2\right)-u\eta\sqrt{1-\eta^2}}{c\left(\xi^2-\eta^2\right)^{3/2}}$$

$$\begin{aligned} D_{\xi\eta} = &\frac{-u\xi\sqrt{\xi^2-1}+(\partial u/\partial\xi)\sqrt{\xi^2-1}\left(\xi^2-\eta^2\right)}{c\left(\xi^2-\eta^2\right)^{3/2}} \\ &+\frac{v\eta\sqrt{1-\eta^2}+(\partial v/\partial\eta)\sqrt{1-\eta^2}\left(\xi^2-\eta^2\right)}{c\left(\xi^2-\eta^2\right)^{3/2}} \end{aligned}$$

$$D_{\eta\eta} = 2\frac{(\partial u/\partial\eta)\sqrt{1-\eta^2}\left(\xi^2-\eta^2\right)+v\xi\sqrt{\xi^2-1}}{c\left(\xi^2-\eta^2\right)^{3/2}}$$

$$D_{\zeta\zeta} = 2\frac{v\xi\sqrt{1-\eta^2}-u\eta\sqrt{\xi^2-1}}{c\sqrt{(\xi^2-1)(\xi^2-\eta^2)(1-\eta^2)}}$$

Note that $D_{\xi\xi}$ and $D_{\xi\eta}$ are identical to eqn (24) in[28]

$$T_{\xi\xi}^\mathrm{H} = 2\left(\frac{\partial v}{h_\xi\partial\xi}+\frac{u}{h_\xi h_\eta}\frac{\partial h_\xi}{\partial\eta}\right), \quad T_{\xi\eta}^\mathrm{H} = \left(\frac{\partial\left(v/h_\eta\right)}{\partial\xi}\frac{h_\eta}{h_\xi}+\frac{\partial(v/h_\xi)}{\partial\eta}\frac{h_\xi}{h_\eta}\right)$$

and $D_{\xi\eta} = D_{\eta\xi}$.

Using eqn (37) and (38), the surface strain tensor is given by

$$\mathbf{D}^\mathrm{s}(\boldsymbol{u}) = \mathbf{P}\cdot\mathbf{D}(\boldsymbol{u})\cdot\mathbf{P} = P_{im}D_{mn}P_{nj}\boldsymbol{e}_i\boldsymbol{e}_i = \begin{pmatrix} 0 & 0 & 0 \\ 0 & D_{\eta\eta}^\mathrm{s} & 0 \\ 0 & 0 & D_{\zeta\zeta}^\mathrm{s} \end{pmatrix},$$

where $D_{\eta\eta}^\mathrm{s} = D_{\eta\eta}$ and $D_{\zeta\zeta}^\mathrm{s} = D_{\zeta\zeta}$.

B.2 Differential operators

The surface gradient operator

$$\nabla_{\mathrm{s}} = \mathbf{P}\cdot\nabla = \mathbf{P}\cdot\begin{bmatrix}\dfrac{1}{h_\xi}\dfrac{\partial}{\partial\xi}\\[2ex] \dfrac{1}{h_\eta}\dfrac{\partial}{\partial\eta}\\[2ex] \dfrac{1}{h_\zeta}\dfrac{\partial}{\partial\phi}\end{bmatrix} = \begin{bmatrix}0\\[1ex] H_{\eta\eta}\dfrac{\partial}{\partial\eta}\\[2ex] H_{\zeta\zeta}\dfrac{\partial}{\partial\xi}\end{bmatrix} \qquad (39)$$

where $H_{\eta\eta} = \dfrac{1}{h_\eta} = \dfrac{\sqrt{1-\eta^2}}{c\sqrt{\xi^2-\eta^2}}$, and $H_{\zeta\zeta} = \dfrac{1}{h_\zeta} = \dfrac{1}{c\sqrt{(\xi^2-1)(1-\eta^2)}}$. The surface Laplacian of velocity is the surface divergence of the surface rate of strain tensor and is given by

$$\nabla_{\mathrm{s}}\cdot\mathbf{D}^{\mathrm{s}}(\boldsymbol{u}) = (\mathbf{P}\cdot\nabla)\cdot(\mathbf{P}\cdot\mathbf{D}(\boldsymbol{u})\cdot\mathbf{P})$$

$$= \begin{bmatrix} -E_{\xi\eta}H_{\eta\eta}D^{\mathrm{s}}_{\eta\eta} - E_{\xi\zeta}H_{\zeta\zeta}D^{\mathrm{s}}_{\zeta\zeta}\\[2ex] E_{\eta\zeta}H_{\zeta\zeta}D^{\mathrm{s}}_{\eta\eta} - E_{\eta\zeta}H_{\zeta\zeta}D^{\mathrm{s}}_{\zeta\zeta} + H_{\eta\eta}\dfrac{\partial D^{\mathrm{s}}_{\eta\eta}}{\partial\eta}\\[2ex] 0\end{bmatrix}, \qquad (40)$$

where

$$E_{ij} = \frac{1}{h_i}\frac{\partial h_j}{\partial x_i}.$$

Appendix C. Effects of large surface viscosities on surface velocity

We discuss the influence of increasing surface dilatational and shear viscosities on the tangential component of the surface viscosity $u_{\mathrm{s}}\cdot t$. Fig. 10 shows $u_{\mathrm{s}}\cdot t$ as a function of the drop surface parameter η in the first quadrant $0 \le \eta \le 1$. We consider the prolate 'A' drop in Fig. 3(a) with $\mathrm{Ca_E} = 0.3$ (a)–(c), and the prolate 'B' drop in Fig. 3(b) with $\mathrm{Ca_E} = 0.4$ (d)–(f).

Fig. 10(a) and (d) show the sole influence of surface dilatational viscosity, (b), (e) show the sole influence of surface shear viscosity, and (c), (f) show the combined effect of the surface viscosities ($\mu_{\mathrm{d}} = 1$ while μ_{s} increases). In all six panels, surface viscosities suppress the surface velocity compared to the clean drop case (dashed curves). In (a), (b) and (d), (e), the velocity is completely suppressed ($u^{\mathrm{t}} \approx 0$) as the viscosities μ_{d}, $\mu_{\mathrm{s}} \gg 1$. As we elaborated in Section 3.2.1, the deformation is larger in (a), (e) and smaller in (b), (d). However, as μ_{d}, $\mu_{\mathrm{s}} \to \infty$ the surface rheology ceases to affect the deformation: the drop becomes immobilized ($u^{\mathrm{t}} \to 0$).

In Fig. 10(c) and (f), the velocity depends on both surface viscosities. The surface shear viscosity is a multiple of $a = \mu_{\mathrm{d}}/20$. Specifically, $\mu_{\mathrm{s}} = 0\,(\bigcirc), 3a\,(\square), 7a\,(\Diamond), 100a\,(\nabla), 1000a\,(\Delta)$, where

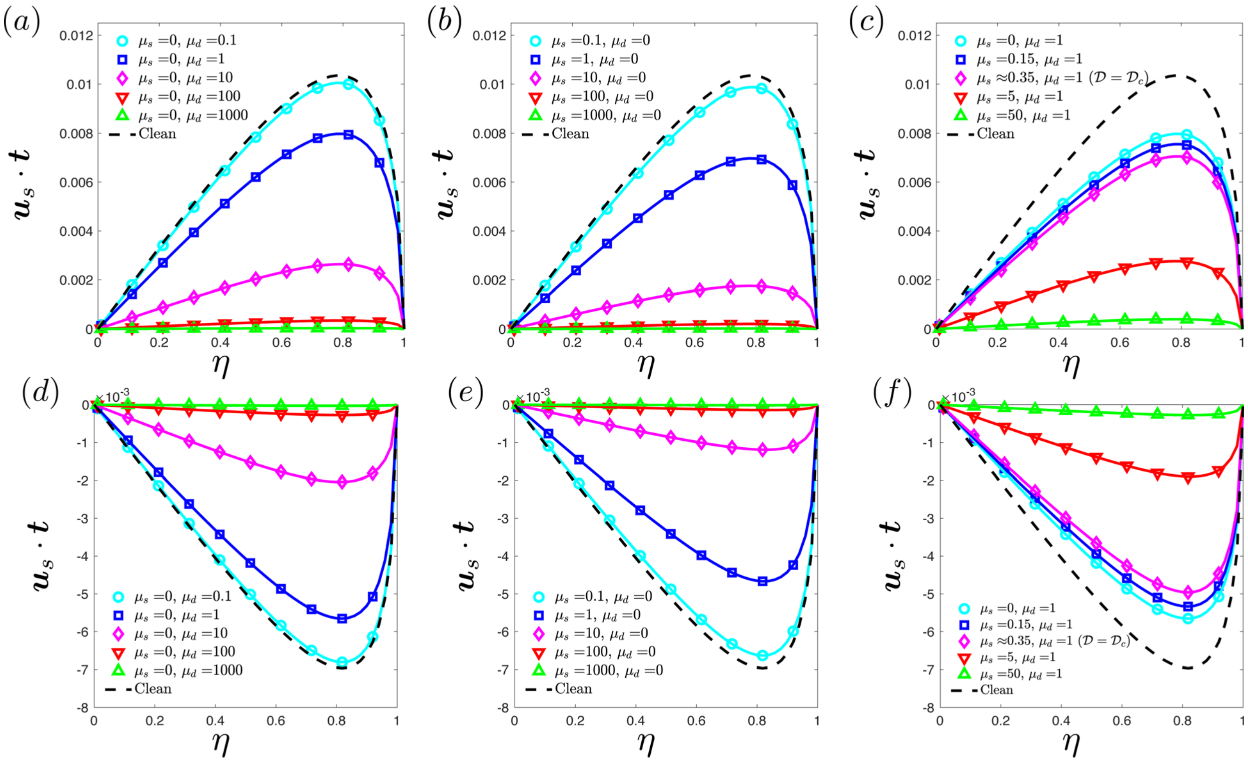

Fig. 10 Tangential component of the surface velocity $u_{\mathrm{s}}\cdot t$ as a function of the drop surface parameter η for the prolate 'A' drop in Fig. 3(a) with $\mathrm{Ca_E} = 0.3$ (a)–(c), and for the prolate 'B' drop in Fig. 3(b) with $\mathrm{Ca_E} = 0.4$ (d)–(f). (a and d) sole influence of surface dilatational viscosity ($\mu_{\mathrm{s}} = 0$); (b and e) sole influence of surface shear viscosity ($\mu_{\mathrm{d}} = 0$); (c and f) combined influence of surface viscosities with $\mu_{\mathrm{d}} = 1$. In all panels, the dashed curves denote the clean drop case.

$7a$ corresponds to $\mathscr{D}/\mathscr{D}_c = 1$ (Section 3.2.2). The strength of the surface velocity determines whether the deformation with combined surface viscosities is larger compared to the clean drop case. For example, considering the prolate 'A' drop, the deformation is larger compared to the clean drop for $\mu_s < 7a$ and smaller otherwise ($\mu_s > 7a$).

Appendix D. Calculation of the critical ratio α

As discussed in Section 3.2.2, certain combinations of surface viscosities yield deformations that are identical compared with those for the clean drop case. By projecting the balance in eqn (18) onto the normal velocity v, the ratio $\alpha \equiv \mu_d/\mu_s$ is given by

$$\alpha = 1 - \frac{\int_S v T^{S}_{\xi\xi} \mathrm{d}S}{\int_S v\kappa\Theta \mathrm{d}S}. \tag{41}$$

This ratio depends on the fluids' electric parameters and on the electric capillary number, as illustrated in Fig. 11: (a) shows the ratio as a function the electric capillary number for the prolate drops in Fig. 5 while (b) presents the same information for prolate 'A' drop with $\sigma_r = 10$, $\varepsilon_r = 25$ and for prolate 'B' drop with $\sigma_r = 100$, $\varepsilon_r = 10^{12}$. For these sets of parameters, we found that $\alpha > 2$ for all values of $\mathrm{Ca_E}$.

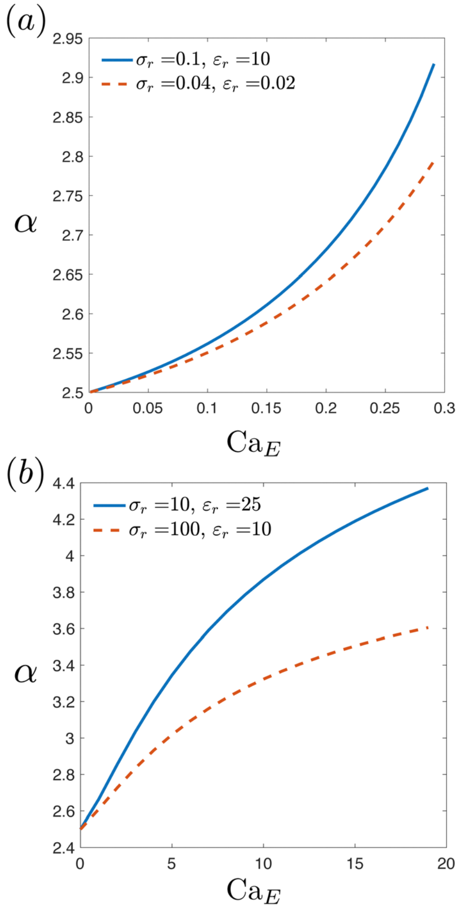

Fig. 11 Critical ratio α from eqn (40) as a function of the electric capillary $\mathrm{Ca_E}$. Blue (◊) curves denote prolate 'A' drops, and red (○) curves denote prolate 'B' drops. The electric parameters are chosen such that the drops (a) ultimately breakup past a critical $\mathrm{Ca_E}$ or (b) keep deforming with larger values of $\mathrm{Ca_E}$.[12] The viscosity ratio $\mu_r = 1$.

Acknowledgements

Funding support by the National Science Foundation (Grant No. 2211633 to H. N., Grant No. 1830958 to O. S. P. and Grant No. 1614863 and 1951600 to Y.-N. Y.) is gratefully acknowledged. H. N. acknowledges support as a Jess and Mildred Fisher Endowed Professor of Mathematics from the Fisher College of Science and Mathematics at Towson University. Y.-N. Y. acknowledges support from the Flatiron Institute, part of Simons Foundation.

Notes and references

1 P. Vlahovska, *Annu. Rev. Fluid Mech.*, 2019, **51**, 305–330.
2 Y. Mori and Y.-N. Young, *J. Fluid Mech.*, 2018, **855**, 67–130.
3 C. T. O'Konski and H. C. Thacher, *J. Chem. Phys.*, 1953, **57**, 955–958.
4 R. S. Allan and S. G. Mason, *Proc. R. Soc. London, Ser. A*, 1962, **267**, 45–61.
5 G. Taylor, *Proc. R. Soc. London, Ser. A*, 1966, **291**, 159–166.
6 J. R. Melcher and G. I. Taylor, *Annu. Rev. Fluid Mech.*, 1969, **1**, 111–146.
7 D. A. Saville, *Annu. Rev. Fluid Mech.*, 1997, **29**, 27–64.
8 J.-W. Ha and S.-M. Yang, *J. Fluid Mech.*, 2000, **405**, 131–156.
9 E. K. Zholkovskij, J. H. Masliyah and J. Czarnecki, *J. Fluid Mech.*, 2002, **472**, 1–27.
10 G. Supeene, C. R. Koch and S. Bhattacharjee, *J. Colloid Interface Sci.*, 2008, **318**, 463–476.
11 J.-W. Ha and S.-M. Yang, *Phys. Fluids*, 2000, **12**, 764.
12 E. Lac and G. M. Homsy, *J. Fluid Mech.*, 2007, **590**, 239.
13 J. A. Lanauze, L. M. Walker and A. S. Khair, *Phys. Fluids*, 2013, **25**, 112101.
14 J. A. Lanauze, L. M. Walker and A. S. Khair, *J. Fluid Mech.*, 2015, **774**, 245.
15 S. Mandal, A. Bandopadhyay and S. Chakraborty, *Phys. Rev. E*, 2016, **93**, 043127.
16 S. Mandal, A. Bandopadhyay and S. Chakraborty, *Phys. Fluids*, 2017, **29**, 012101.
17 D. Das and D. Saintillan, *J. Fluid Mech.*, 2017, **810**, 225.
18 N. Bentenitis and S. Krause, *Langmuir*, 2005, **21**, 6194–6209.
19 J. Zhang, J. D. Zahn and H. Lin, *Phys. Rev. E: Stat., Nonlinear, Soft Matter Phys.*, 2013, **87**, 043008.
20 M. Zabarankin, *SIAM J. Appl. Math.*, 2013, **73**, 677–699.
21 M. Zabarankin, *SIAM J. Appl. Math.*, 2016, **76**, 1606–1632.
22 P. R. Brazier-Smith, *Phys. Fluids*, 1971, **14**, 1.
23 P. R. Brazier-Smith, S. G. Jennings and J. Latham, *Proc. R. Soc. London, Ser. A*, 1971, **325**, 363–376.
24 M. Miksis, *Phys. Fluids*, 1981, **24**, 1967.
25 O. A. Basaran and L. E. Scriven, *Phys. Fluids*, 1989, **1**, 799.

26 H. Nganguia, Y.-N. Young, A. T. Layton, W.-F. Hu and M.-C. Lai, *Commun. Comput. Phys.*, 2015, **18**, 429–449.

27 W.-F. Hu, M.-C. Lai and Y.-N. Young, *J. Comput. Phys.*, 2014, **282**, 47–61.

28 H. Nganguia, Y.-N. Young, P. M. Vlahovska, J. Bławzdziewcz, J. Zhang and H. Lin, *Phys. Fluids*, 2013, **25**, 092106.

29 H. Nganguia, O. S. Pak and Y.-N. Young, *Phys. Rev. E*, 2019, **99**, 063104.

30 C. Sorgentone, A.-K. Tornberg and P. Vlahovska, *J. Comput. Phys.*, 2019, **389**, 111–127.

31 H. Nganguia, W. F. Hu, M.-C. Lai and Y. N. Young, *Phys. Rev. Fluids*, 2021, **6**, 064004.

32 P. Erni, P. Fischer and E. J. Windhab, *Appl. Phys. Lett.*, 2005, **87**, 244104.

33 P. Erni, *Soft Matter*, 2011, **7**, 7586.

34 M. A. Herrada, A. Ponce-Torres, M. Rubio, J. Eggers and J. M. Montanero, *J. Fluid Mech.*, 2022, **934**, A26.

35 A. R. Honerkamp-Smith, F. G. Woodhouse, V. Kantsler and R. E. Goldstein, *Phys. Rev. Lett.*, 2013, **111**, 038103.

36 R. W. Flumerfelt, *J. Colloid Interface Sci.*, 1980, **76**, 330–349.

37 V. Narsimhan, *J. Fluid Mech.*, 2019, **862**, 385–420.

38 N. Singh and V. Narsimhan, *Phys. Rev. Fluids*, 2020, **5**, 063601.

39 J. Gounley, G. Boedec, M. Jaeger and M. Leonetti, *J. Fluid Mech.*, 2016, **791**, 464–494.

40 Z. Y. Luo, X. L. Shang and B. F. Bai, *J. Fluid Mech.*, 2018, **858**, 91–121.

41 N. Singh and V. Narsimhan, *J. Fluid Mech.*, 2021, **927**, A44.

42 N. Singh and V. Narsimhan, *J. Fluid Mech.*, 2022, **946**, A24.

43 J. Li and H. Manikantan, *Phys. Rev. Fluids*, 2021, **6**, 074001.

44 A. Ponce-Torres, M. Rubio, M. A. Herrada, J. Eggers and J. M. Montanero, *Sci. Rep.*, 2020, **10**, 16065.

45 H. Wee, B. W. Wagoner, V. Garg, P. M. Kamat and O. A. Basaran, *J. Fluid Mech.*, 2020, **908**, A38.

46 H. Wee, B. W. Wagoner and O. A. Basaran, *Phys. Rev. Fluids*, 2022, **7**, 074001.

47 S. Mandal and S. Chakraborty, *Phys. Fluids*, 2017, **29**, 052002.

48 Y. Han, J. Koplik and C. Maldarelli, *J. Colloid Interface Sci.*, 2021, 900–911.

49 P. M. Vlahovska, R. S. Gracia, S. Aranda-Espinoza and R. Dimova, *Biophys. J.*, 2009, **96**, 4789.

50 P. F. Salipante and P. M. Vlahovska, *Phys. Fluids*, 2010, **22**, 112110.

51 J.-W. Ha and S.-M. Yang, *J. Colloid Interface Sci.*, 1995, **175**, 369–385.

52 J.-W. Ha and S.-M. Yang, *J. Colloid Interface Sci.*, 1998, **206**, 195–204.

53 P. F. Salipante and P. M. Vlahovska, *Phys. Rev. E: Stat., Nonlinear, Soft Matter Phys.*, 2013, **88**, 043003.

54 S. Torza, R. G. Cox and S. G. Mason, *Proc. R. Soc. London, Ser. A*, 1971, **269**, 295–319.

55 D. Das and D. Saintillan, *J. Fluid Mech.*, 2017, **829**, 127.

56 J. Q. Feng, *Proc. R. Soc. London, Ser. A*, 1999, **455**, 2245–2269.

57 L. E. Scriven, *Chem. Eng. Sci.*, 1960, **12**, 98–108.

58 N. Dubash and A. J. Mertel, *J. Fluid Mech.*, 2007, **581**, 469.

59 M. Zabarankin, *SIAM J. Appl. Math.*, 2013, **73**, 677–699.

60 M. Zabarankin, *SIAM J. Appl. Math.*, 2016, **76**, 1606–1632.

61 M. Zabarankin and Y. Zhang, *SIAM J. Appl. Math.*, 2021, **81**, 2180–2194.

62 G. I. Taylor, *Proc. R. Soc. London, Ser. A*, 1964, **280**, 383–397.

63 G. Dassios, M. Hadjinicolaou and A. C. Payatakes, *Q. Appl. Math.*, 1994, **52**, 157–191.

64 G. Dassios, M. Hadjinicolaou, F. A. Coutelieris and A. C. Payatakes, *Int. J. Eng. Sci.*, 1995, **33**, 1465–1490.

65 J. D. Sherwood, *J. Fluid Mech.*, 1988, **188**, 133–146.

66 K. Danov, R. Aust, F. Durst and U. Lange, *J. Colloid Interface Sci.*, 1995, **175**, 36–45.

67 M. Pourali, N. O. Jaensson and M. Kröger, *J. Fluid Mech.*, 2021, **924**, A30.

68 J. Kragel, G. Kretzschmar, J. B. Li, G. Loglio, R. Miller and H. Mohwald, *Thin Solid Films*, 1996, **284**, 361–364.

69 K. Kim, S. Q. Choi, J. A. Zasadzinski and T. M. Squires, *Soft Matter*, 2011, **7**, 7782–7789.

70 T. Verwijlen, P. Moldenaers and J. Vermant, *Eur. Phys. J.: Spec. Top.*, 2013, **222**, 83–97.

71 Z. A. Zell, A. Nowbahar, V. Mansard, L. G. Leal, S. S. Deshmukh, J. M. Mecca, C. J. Tucker and T. M. Squires, *Proc. Natl. Acad. Sci. U. S. A.*, 2014, **111**, 3677–3682.

72 J. R. Samaniuk and J. Vermant, *Soft Matter*, 2014, **10**, 7023–7033.

73 N. F. Djabbarah and D. T. Wasan, *Chem. Eng. Sci.*, 1982, **37**, 175–184.

74 X. Xu and G. M. Homsy, *J. Fluid Mech.*, 2006, **564**, 395.